HiHiMap: single-cell quantitation of histones and histone posttranslational modifications across the cell cycle by high-throughput imaging

Linda Zane[a], Fleur Chapus[a], Gianluca Pegoraro[b], and Tom Misteli[a,*]
[a]Cell Biology of Genomes and [b]NCI High-Throughput Imaging Facility, National Cancer Institute, National Institutes of Health, Bethesda, MD 20892

ABSTRACT **We describe High-throughput Histone Mapping (HiHiMap), a high-throughput imaging method to measure histones and histone posttranslational modifications (PTMs) in single cells. HiHiMap uses imaging-based quantification of DNA and cyclin A to stage individual cells in the cell cycle to determine the levels of histones or histone PTMs in each stage of the cell cycle. As proof of principle, we apply HiHiMap to measure the level of 21 core histones, histone variants, and PTMs in primary, immortalized, and transformed cells. We identify several histone modifications associated with oncogenic transformation. HiHiMap allows the rapid, high-throughput study of histones and histone PTMs across the cell cycle and the study of subpopulations of cells.**

Monitoring Editor
Susan Strome
University of California, Santa Cruz

Received: Dec 21, 2016
Revised: Jun 8, 2017
Accepted: Jun 9, 2017

INTRODUCTION

Histones are among the most evolutionarily conserved proteins in eukaryotic cells. Two copies of each core histone (H2A, H2B, H3, and H4) are assembled into octamers around which 147 base pairs of DNA are wrapped to form nucleosomes, the basic structural units of chromatin (Kornberg and Lorch, 1999). Histones are extensively modified on their N-terminal tails by posttranslational modifications (PTMs), including phosphorylation on serine or threonine residues, methylation on lysine or arginine, acetylation, ubiquitylation, and SUMOylation on lysine (Zhang *et al.*, 2002; Tan *et al.*, 2011). These modifications exert biological functions by affecting the recruitment of histone-binding proteins, such as chromatin remodelers or chromatin structural proteins (Swygert and Peterson, 2014; Tessarz and Kouzarides, 2014; Wike *et al.*, 2016). Although some histone PTMs are known to be associated with active chromatin states, others are indicative of repressive chromatin (Jenuwein and Allis, 2001; Rothbart and Strahl, 2014). In addition to histone PTMs, histone variants also play an important role in the regulation of chromatin organization—for example, the replacement of canonical histones by nonallelic variants modifies nucleosome stability and chromatin dynamics (Weber and Henikoff, 2014). Histone variants and PTMs are important for regulation of basic genomic processes, including the DNA damage response, transcription, and replication (House *et al.*, 2014; Teves *et al.*, 2014; Polo and Almouzni, 2015; Venkatesh and Workman, 2015; Almouzni and Cedar, 2016). Owing to their role in gene regulation and genome stability, histone variants and modifications have been implicated in carcinogenesis (Seligson *et al.*, 2005, 2009; Elsheikh *et al.*, 2009; Sharma *et al.*, 2010; Zane *et al.*, 2014).

To maintain sufficient levels of histones to ensure normal chromosomal DNA compaction throughout the cell cycle, the synthesis of DNA and of core histones is tightly coordinated. Core histone protein levels double via transcriptional and posttranscriptional upregulation during the cell cycle as the genome is duplicated in S phase (Osley, 1991; Marzluff and Duronio, 2002; Marzluff *et al.*, 2008; Nelson *et al.*, 2002).

PTMs must be reestablished on newly synthesized histones after DNA replication (Loyola *et al.*, 2006; Scharf *et al.*, 2009; Budhavarapu *et al.*, 2013; Alabert *et al.*, 2015). In contrast to the histone proteins, histone PTMs rapidly turn over via action of histone-modifying enzymes and may thus fluctuate between individual cells, during the cell cycle, and within a cell cycle phase. The standard methods to analyze histones and histone PTMs are Western blotting and stable

This article was published online ahead of print in MBoC in Press (http://www.molbiolcell.org/cgi/doi/10.1091/mbc.E16-12-0870) on June 14, 2017.

*Address correspondence to: Tom Misteli (mistelit@mail.nih.gov).

Abbreviations used: HiHiMap, High-throughput Histone Mapping; PTM, posttranslational modification.

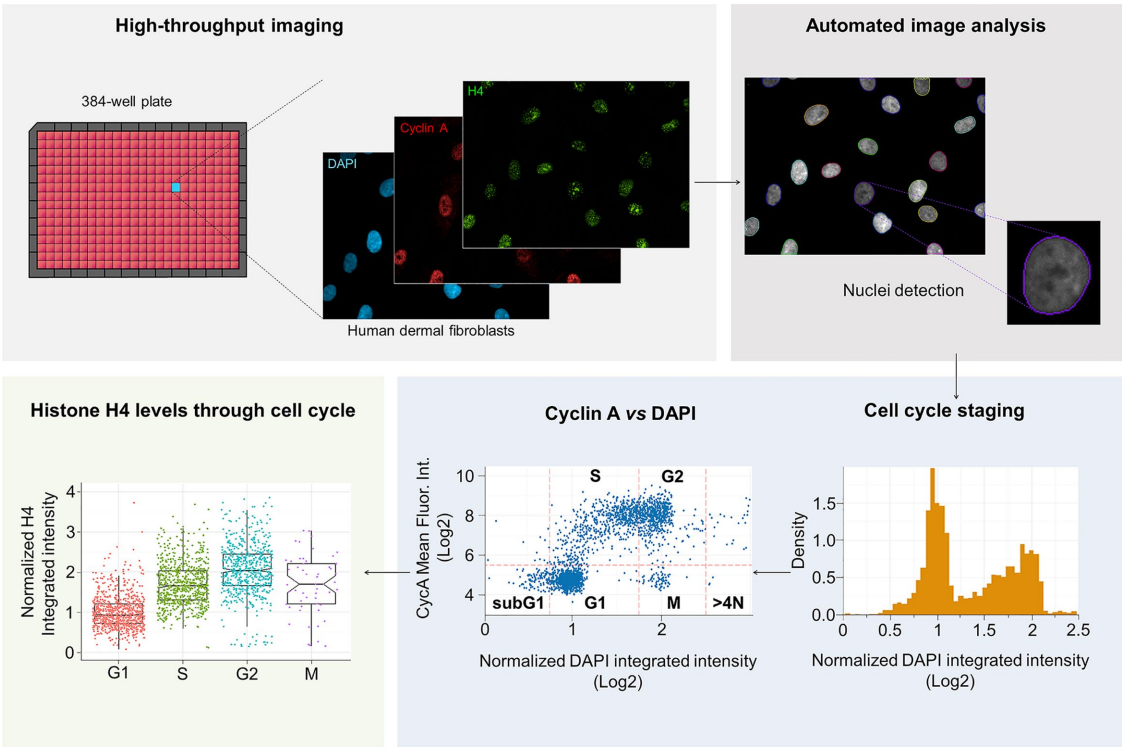

FIGURE 1: Outline of the HiHiMap method. Cells are plated in 384-well plates, fixed, and nuclei are stained with DAPI. Cells are incubated in the presence of an antibody against cyclin A and an antibody against a specific histone or histone PTMs of interest. Images of stained cells are acquired in two dimensions using a high-throughput confocal microscope, and automated image analysis is used to calculate the averaged integrated and mean fluorescence intensities of DAPI, cyclin A, and histone/PTM of interest in three different channels for each cell. The histograms of DNA content in the cell population are then calculated to generate cell cycle profiles using R. The first peak represents the G1 cell population, and its position is set to a value of 1. Cells in the G2 phase are distinguished from the cells in mitosis using a cyclin A intensity threshold in addition to the DAPI cutoffs. The single-cell level of normalized fluorescence intensity for a histone or a histone modification is represented for each cell cycle phase. Each dot represents one individual cell.

isotope labeling with amino acids in cell culture (SILAC)–based quantitative mass spectrometry (MS; Ong *et al.*, 2002; Pesavento *et al.*, 2008; Scharf *et al.*, 2009; Sweet *et al.*, 2010; Zee *et al.*, 2010; Xu *et al.*, 2012). These methods are limited, in that they are only able to provide a population-based average measurement of histone levels or PTMs and are unable to detect differences among subpopulations or individual cells. Although they can be used for analysis of cell cycle fluctuations when combined with cell cycle synchronization methods, synchronization may affect the levels of some histones and histone PTMs. For SILAC-MS analysis, the labeling step requires extensive culturing of cells over several days. Both Western blotting and SILAC-MS require relatively large numbers of cells. In addition, these approaches cannot be easily scaled up for the parallel analysis of a large number of samples. This makes them unsuitable for a screening or eventually diagnostic or prognostic purposes.

To overcome these limitations, we developed High-throughput Histone Mapping (HiHiMap), a rapid method for single-cell quantification of histone and histone PTM levels throughout the cell cycle. The approach is based on high-throughput imaging and uses cyclin A immunofluorescence (IF) and 4′,6-diamidino-2-phenylindole (DAPI) DNA staining for cell cycle staging, which allows the determination of the cell cycle stage of individual cells without the need for cell synchronization and, simultaneously, the measurement of histones and histone PTM levels at the single-cell level. The high-throughput nature of the method allows for parallel analysis of multiple histone PTMs in a single experiment. Using HiHiMap, we examined 21 histones and histone modifications in an oncogenic cellular transformation model (Hahn *et al.*, 1999, 2002; Elenbaas *et al.*, 2001; Scaffidi and Misteli, 2011) and identified single cell–level changes of several histone variants and PTMs during oncogenic transformation.

RESULTS

HiHiMap outline

We sought to develop a rapid method to measure the levels of histones and histone PTMs through the cell cycle at the single-cell level and in a high-throughput format to enable comprehensive analysis of the epigenetic landscape. HiHiMap is a high-throughput imaging-based approach in which a combination of DAPI and cyclin A staining is used to stage individual cells in the cell cycle, and this information is combined with the use of antibody-based quantitative detection of histones and histone PTMs in the same individual cells (Figure 1).

For HiHiMap, cells are plated in 384-well imaging plates, fixed in 4% paraformaldehyde (PFA), and stained for cyclin A and a histone or histone PTM of interest for each well using specific antibodies (see *Materials and Methods*). For analysis, ~1500 cells in 50 randomly selected fields per well are imaged in multiple fluorescence channels using automated microscopy (see *Materials and Methods*). High-content image analysis is then used to segment the nuclei using the DAPI channel; in addition, averaged integrated DAPI, mean cyclin A, and integrated histone or histone PTM fluorescence

intensities are measured in three separate channels (DAPI, Alexa 488, Alexa 647) over the nuclear mask generated in the segmentation step (see *Materials and Methods*). Each nucleus is assigned to a cell cycle stage based on integrated DAPI intensity and cyclin A staining, and the corresponding histone or histone PTM levels are measured in each cell cycle–staged nucleus. Results are represented as single-cell data sets (Figure 1). As proof of principle, HiHiMap is applied to the analysis of 25 histones, histone variants, and histone PTMs in hTERT immortalized CRL-1474 human dermal fibroblasts (HDFs; Scaffidi and Misteli, 2011; Fernandez *et al.*, 2014; Supplemental Table S1).

Cell cycle staging

Single cells are staged in the cell cycle by measurement of the integrated DAPI intensity of an individual cell nucleus, as previously described (Roukos *et al.*, 2015). This approach of cell cycle staging gives similar results as fluorescence-activated cell sorting analysis (Roukos *et al.*, 2015; Supplemental Figure S4). Typical imaging-based DAPI intensity distributions are biphasic, with peak 1 representing G1 cells and peak 2 representing G2/M cells (Roukos *et al.*, 2015). Although the relative position of peaks 1 and 2 is generally constant, the absolute position of these peaks on the *x*-axis, ($\log_2$ integrated DAPI intensity), can slightly vary from well to well, possibly due to variations in DAPI staining and/or illumination. To compensate for these fluctuations and compare cell cycle distributions from independent wells, we normalized the integrated DAPI intensity for each well by assigning the value of 1 to the position of peak 1 estimated by using a mixed model algorithm in the statistical software R (for details, see *Materials and Methods*). In addition, to better distinguish cells in each cell cycle phase, we used a combination of gates based on both the normalized integrated DAPI intensity and the cyclin A mean intensity, which is known to be elevated in S and G2 phases (Pagano *et al.*, 1992). Using these empirically determined gates, G1 cells were defined as having normalized DAPI intensity value between 0.75 and 1.75 while being cyclin A negative, S-phase cells as having DAPI intensity of 0.75–1.75 and being cyclin A positive, G2 cells as having DAPI intensity of 1.75–2.5 and being cyclin A positive, and M-phase cells as having DAPI intensity 1.75–2.5 and being cyclin A negative (Supplemental Figure S1A).

HiHiMap validation using core histones

To validate HiHiMap, we measured the levels of three nuclear proteins with known cell cycle behavior in hTERT immortalized CRL-1474 HDFs (Scaffidi and Misteli, 2011; Fernandez *et al.*, 2014). Histone H4 is a core histone whose intensity level is known to follow DNA content during the cell cycle (Osley, 1991; Marzluff and Duronio, 2002; Marzluff *et al.*, 2008). As expected, histone H4 levels increase 1.9 ± 0.03-fold (mean ± SEM) and 2.3 ± 0.03-fold in S and G2 phases, respectively, in comparison to G1-phase cells (Figure 2, B and C). Results were highly reproducible in both technical and biological replicates (Supplemental Figure S2A), and similar results were observed with two different commercial antibodies directed against H4 (Supplemental Table S1 and Supplemental Figure S2B). Computational simulation of 10,000 comparisons of variable population sizes generated by random subsampling of cells in G1 was used to determine that the minimally required sample size to achieve statistical confidence (>95%) is ~230 cells per cell cycle stage per well (Kolmogorov–Smirnov [KS] test; $p < 0.005$; Supplemental Figure S1C; see *Materials and Methods* for details).

Phosphorylation on serine 10 of histone H3 (H3S10Ph) is a well-characterized mitotic marker (Sawicka and Seiser, 2012). As expected, a major increase of H3S10ph levels was found in G2/M phase (9.2 ± 0.7-fold) in comparison to G1 cells (Figure 2, E and F). As a negative control, the transcription factor LHX9, involved in brain development (Vladimirova *et al.*, 2009), did not vary with DNA levels in HDFs, and we observe only a marginal increase in the LHX9 level during the cell cycle (ratio S/G1 = 1.2 ± 0.01; G2/G1 = 1.3 ± 0.02; and M/G1 = 1.5 ± 0.08; Figure 2, H and I).

Analysis of the levels of core histones and variants during the cell cycle

To extend our analysis of histones, we measured the levels of three core histones (Figure 3A) and their variants (Figure 3B). Protein levels of H2A, H3, and H4 increased in S phase by 1.7 ± 0.02-, 2 ± 0.03-, and 1.87 ± 0.03-fold, respectively, and by 2.3 ± 0.03-, 2.6 ± 0.04-, 2.3 ± 0.03-fold, respectively, in G2 phase relative to G1 before decreasing 1.7 ± 0.09-, 1.6 ± 0.09-, and 1.7 ± 0.09-fold during mitosis in comparison to G2 phase (Figure 3A). Despite the slight differences observed in the variations of histone levels between histones, most likely due to the antibody quality, we conclude that HiHiMap detects cell cycle–related fluctuations in histone levels.

In contrast to canonical histones, the synthesis of histone variants is uncoupled from DNA replication (Talbert and Henikoff, 2010). Thus, to further validate our method, we applied HiHiMap to characterize the cell cycle behavior of several histone variants (Figure 3B). Levels of the H3 variant H3.3 and the H2A variant H2AZ, respectively, increased 1.2 ± 0.03- and 1.2 ± 0.01-fold from G1 to S phase and 1.4 ± 0.04- and 1.4 ± 0.02-fold to G2 before reaching a 1.5 ± 0.16- and 1.9 ± 0.09-fold increase in M phase (Figure 3B), suggesting that these variants are incorporated throughout the cell cycle. MacroH2A1 showed no increase from G1 to S and G2 phases (S/G1 = 0.9 ± 0.02; G2/G1 = 1 ± 0.03), followed by a 1.7 ± 0.12-fold increase between G2 and M, suggesting that macroH2A variants are preferentially incorporated into chromatin after DNA replication and are not incorporated significantly during S phase. Of interest, in contrast to other histone variants, H2AX showed larger fluctuations from G1 to S and to G2, with 1.4 ± 0.02- and 1.7 ± 0.03-fold increases, respectively, followed by a slight decrease in mitosis (1.6 ± 0.07-fold decrease). The H2AX results suggest mechanisms of chromatin assembly during DNA replication. This is consistent with the H2AX gene (*H2AFX*) containing features of both replication-dependent and replication-independent histone species. In particular, *H2AFX* is a small, intron-less gene and has the stem–loop structure characteristic of replication-linked histones (Mannironi *et al.*, 1989). We conclude that, in contrast to core histones, levels of several histone variants, except H2AX, do not follow cellular DNA levels.

Characterization of cell cycle fluctuations of histone modifications

Histones undergo extensive PTMs (Zhang *et al.*, 2002; Tan *et al.*, 2011). The kinetics of histone modifications during the cell cycle are relatively poorly characterized, in part due to the difficulty in generating cell cycle–staged cell populations for biochemical analysis and to the heterogeneity of modifications among individual cells. We used HiHiMap to characterize the cell cycle–related fluctuations of 17 histone modifications and determine the variability of modifications between individual cells in the same cell cycle phase.

Using a set of commercially available antibodies, some of which were validated (Egelhofer *et al.*, 2011; Supplemental Table S1), we detected the rapid increase after DNA replication of several H3K4 methylation events. S/G1 ratios of monomethlyation, dimethylation, and trimethylation of H3K4 were increased 1.7 ± 0.03-, 1.4 ± 0.02-, and 1.4 ± 0.01-fold, respectively, to reach a 2-fold increase in

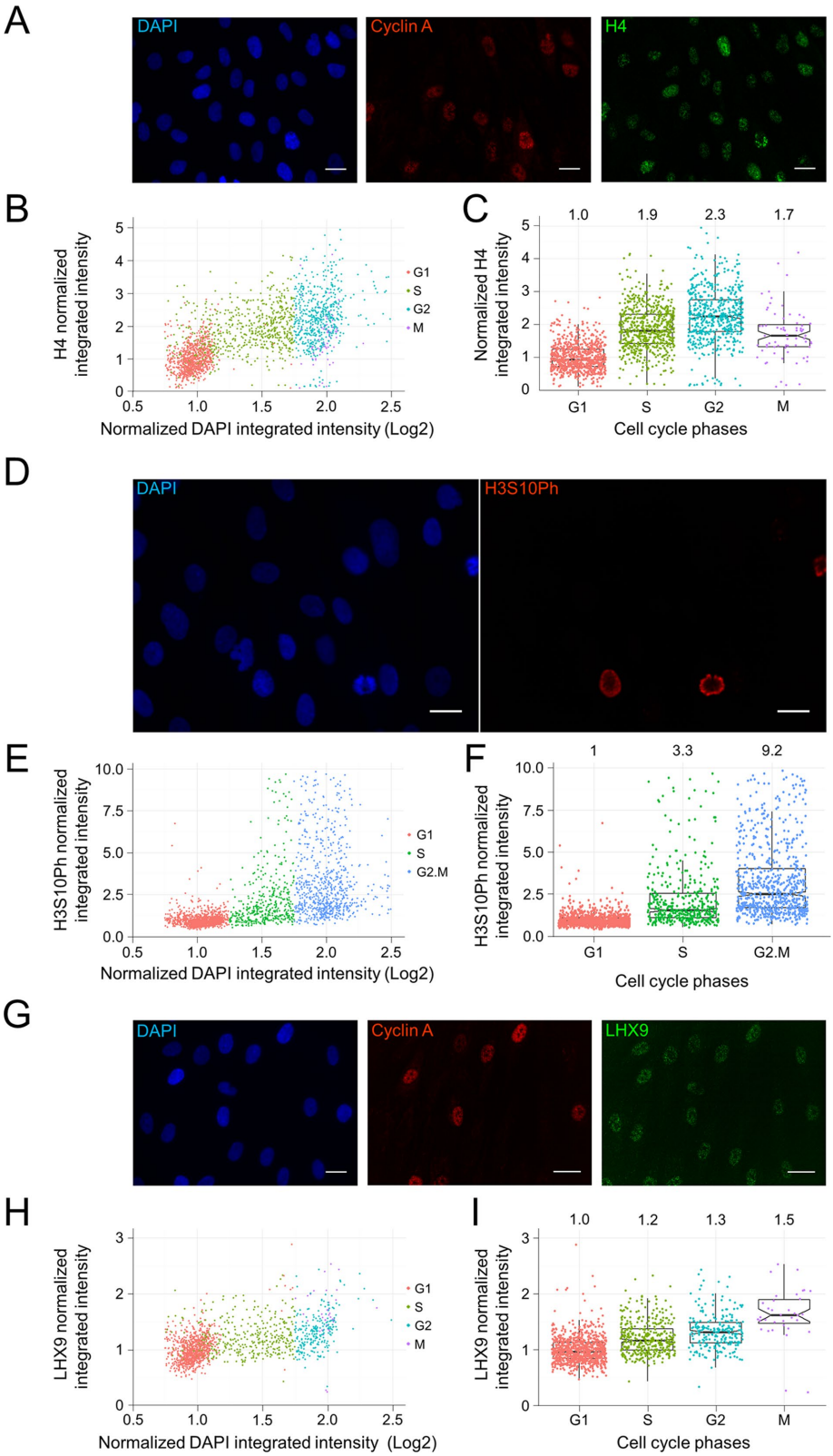

FIGURE 2: Proof of principle of HiHiMap. Representative confocal images of (A) H4, a core histone, (D) H3S10Ph, a mitotic histone PTM, and (G) LHX9, a non–cell cycle–regulated transcription factor involved in brain development, and their cyclin A (far red) and/or DAPI staining (blue) in immortalized HDFs. Scale bar, 10 µm. Single-cell levels of H4 (B, C), H3S10Ph (E, F), and LHX9 (H, I) as a function of DNA amount (DAPI intensity level) and at each cell cycle stage. Each dot represents a single cell. In box plots, the line corresponds to the median, notches represent the estimated 95% CI for the median, the lower and upper hinges of the box plot indicate the 25th and 75th percentiles, respectively, and the whiskers correspond to ± 1.5 × IQR of the hinge, where IQR is the interquartile range or distance between the first and third quartiles. The numbers above the box plots represent the mean fold change compared with G1 levels. Each graph represents the results of two technical replicates. Scale bar, 20 µm.

G2 (H3K4-me1: ratio S/G1 = 2.1 ± 0.04; -me2: 1.9 ± 0.04; -me3: 1.9 ± 0.02) and then decreased in mitosis (ratio M/G1: 1.4 ± 0.1-fold, 1.7 ± 0.18 –fold, and 1.5 ± 0.1-fold for monomethlyation, dimethylation, and trimethylation, respectively; Figure 4A). The level of H3K9me1, commonly associated with transcriptional activation (Barski *et al.*, 2007), followed the same pattern as H3K4 methylation during the cell cycle, with its highest level in G2 phase (ratio S/G1 = 1.2 ± 0.01: ratio G2/G1 = 1.9 ± 0.04; ratio M/G1 = 1.6 ± 0.1; Figure 4A). In contrast, the higher methylation states of H3K9, which are linked to transcriptional repression (Noma *et al.*, 2001), modestly increased from G1 to S (ratio S/G1 = 1.2 ± 0.01 for H3K9me2 and 1.3 ± 0.02 for H3K9me3; Figure 4A), and for H3K9me2 and H3K9me3, we observed 1.5 ± 0.02- and 1.4 ± 0.02-fold increases, respectively, in G2 phase and 1.8 ± 0.07- and 2 ± 0.01-fold increases, respectively, in M phase compared with G1 (Figure 4A). H3K27me3, one of the most prominent repressive histone marks (Barski *et al.*, 2007; Schlesinger *et al.*, 2007), increased by 1.6 ± 0.03- and 1.7 ± 0.04-fold in S and G2 phases, respectively, before dropping off to a 1.3 ± 0.08-fold increase in mitosis in comparison to G1 (Figure 4A). H3K36me3, which is enriched in the transcribed regions of active genes (Kolasinska-Zwierz *et al.*, 2009; Chantalat *et al.*, 2011), slightly increases during the cell cycle (ratios S/G1: 1.12 ± 0.02; G2/G1: 1.24 ± 0.02) before a 1.61 ± 0.01-fold increase in mitosis compared with G1 (Figure 4A). Furthermore, monomethylated and dimethylated H4K20, involved in DNA replication and DNA repair (Beck *et al.*, 2012a,b; Jorgensen *et al.*, 2013), modestly increased from G1 into S phase (ratios S/G1: 1.2 ± 0.03 for H4K20me1 and 1.1 ± 0.01 for H4K20me2) before increasing in G2 phase (ratio G2/G1: 2.5 ± 0.08) for H4K20me1 and in mitosis for H4K20me2 (1.73 ± 0.09; Figure 4B). Similar results were obtained with a different antibody against H4K20me2 (Supplemental Figure S2C).

In contrast to histone methylation, analysis by HiHiMap of H3K9Ac, H4K5Ac, and H3 and H4 global acetylation levels showed increases between G1 and S phases (ratio S/G1 = 1.5 ± 0.02 for H3K9Ac; 1.5 ± 0.02 for H4K5Ac; 1.5 ± 0.03 for H3Ac; 1.5 ± 0.02 for

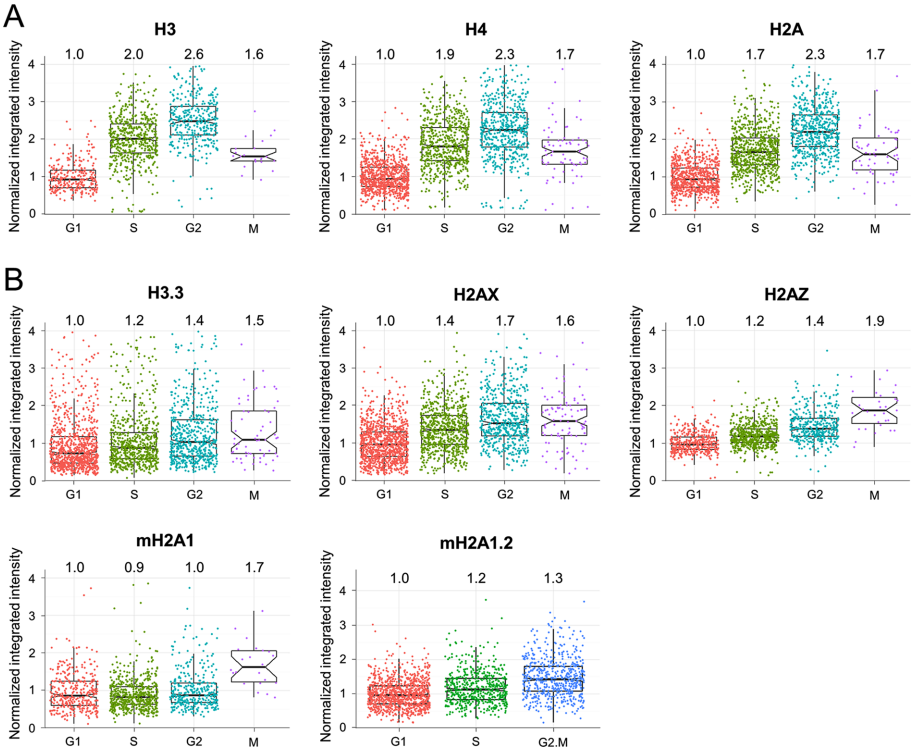

FIGURE 3: Single-cell levels of (A) core histones and (B) histone variants during the cell cycle. Each dot represents the level of the histone or histone modification of interest in a single cell. In box plots, the line corresponds to the median, notches represent the estimated 95% CI for the median, the lower and upper hinges of the box plot indicate the 25th and 75th percentiles, respectively, and the whiskers correspond to ± 1.5 × IQR of the hinge, where IQR is the interquartile range or distance between the first and third quartiles. The numbers above the box plots represent the mean fold change compared with G1 levels. Each graph represents the results of two technical replicates.

H4Ac), and increased further after DNA synthesis, leading to a 2-fold ratio between G2 and G1 phases (ratio G2/G1 = 2 ± 0.02 for H3K9Ac; 2 ± 0.04 for H4K5Ac; 2.1 ± 0.04 for H3Ac; 1.9 ± 0.04 for H4Ac), followed by a slight decrease in mitosis (ratio M/G1 = 1.86 ± 0.07 for H3K9Ac; 1.73 ± 0.01 for H4K5Ac; 1.7 ± 0.13 for H3Ac; 1.6 ± 0.09 for H4Ac; Figure 4, C and D). As expected, treatment with the histone deacetylase inhibitor trichostatin A (TSA) (Ugarte *et al.*, 2015) resulted in a marked increase in the levels of H3Ac, H3K9Ac, and H3K56Ac and concomitant cell cycle changes (Supplemental Figure S3)

These observations delineate the cell cycle behavior of a comprehensive sets of histone modifications at the single-cell level.

Identification of dysregulated histones and histone PTMs during oncogenic transformation

To apply HiHiMap to a biological problem, we took advantage of the capacity of HiHiMap to systematically analyze histones and histone modifications during oncogenic transformation. To generate transformed cells, we transduced primary human skin fibroblasts from three individuals with a combination of lentiviral vectors expressing hTERT, H-RasV12, and SV40 Large-T (LT) and Small-T (ST) antigens as previously described (Hahn *et al.*, 1999, 2002; Elenbaas *et al.*, 2001; Scaffidi and Misteli, 2011; Supplemental Figure S4). We confirmed the presence of the three transgenes at the RNA (Supplemental Figure S4A) and protein (Supplemental Figure S4B) levels and their ability to form colonies in soft agar at high rates (Supplemental Figure S4C). Comparative profiling of the cell cycle distribution of primary, hTERT-immortalized, and transformed cells by DAPI staining revealed the expected high levels of polyploidy in the transformed cells, with the shift of the cell cycle profile toward higher levels of integrated DAPI intensity (Supplemental Figures S5 and S6). These results were confirmed by flow cytometry (Supplemental Figure S5).

To account for the tetraploid nature of transformed cells, the DAPI thresholds to stage cells were modified, and diploid G2 cells were defined as cells with DAPI intensity of 1.75–2.25 and cyclin A positive and tetraploid cells in G1 phase as DAPI intensity of 1.75–2.25 and cyclin A negative. Tetraploid cells in S phase were defined as DAPI intensity of 2.25–2.75 and cyclin A positive and tetraploid cells in G2 as DAPI intensity of 2.75–3.25 and cyclin A positive (Supplemental Figure S7). The ploidy status of the transformed cells was confirmed by flow cytometry to correctly assign cell cycle stages in these samples (Supplemental Figure S6). We also observed that transformed cells exhibited higher background levels of cyclin A, and so we adjusted thresholds accordingly (Supplemental Figure S8). To account for the variability in genetic material between individual cells, histone levels were normalized to the amount of DNA in each cell.

The values of 21 histone variants and modifications of primary, immortalized, and transformed cells are represented as a heat map in Figure 5. We normalized the levels of core histones and histone variants to the DNA content (Figure 5C). We observed an increase of 2.1 ± 0.02-, 1.5 ± 0.07-, 1.5 ± 0.04-, and 2.7 ± 0.03-fold in the level of H2AX variant after normalization to DNA amount in G1, S, G2, and M, respectively, between the primary and transformed cells ($p < 10^{-14}$ for each cell cycle stage, Student's *t* test with Benjamini–Hochberg multiple testing correction) and an increase of 2.6 ± 0.03-, 1.7 ± 0.05, 1.8 ± 0.03-, and 3.3 ± 0.08-fold in the level of this variant between the immortalized cells and their transformed counterparts in G1, S, G2, and M ($p < 10^{-16}$, Student's *t* test), respectively (Figures 5C and 6A). We observed a slight decrease of 0.81 ± 0.04- ($p < 10^{-16}$), 0.87 ± 0.15- ($p = 0.07$), 0.81 ± 0.09- ($p = 4.6 \times 10^{-5}$), and 0.82 ± 0.11- ($p = 0.001$, Student's *t* test) fold in the levels of H2AX between the primary and immortalized cells in G1, S, G2, and M phases, respectively. Representative results for a single cell line (AG06310) are shown, and all results were confirmed in three independent experiments in the same cell line and in HDFs from additional individuals (Supplemental Figures S9C and S10C).

For analysis of modifications of histones H3 and H4, we normalized their intensity levels to the intensity levels of the DNA content to account for the observed polyploidy in individual cells. Then, because the intensity levels of core histones vary between samples (Supplemental Figures S13–S15), we normalized them to the corresponding core histone (Figure 5, A and B). After normalization to DNA content and H3, H3K9me2 levels were decreased by 0.46 ± 0.03- ($p < 10^{-16}$), 0.44 ± 0.47- ($p = 0.067$), 0.62 ± 0.05- ($p < 10^{-16}$), and 0.51 ± 0.06- ($p < 10^{-16}$) fold between primary and transformed cells and by 0.55 ± 0.03- ($p < 10^{-16}$), 0.77 ± 0.5 ($p = 0.006$), 0.83 ± 0.05- ($p = 5.5 \times 10^{-7}$), and 0.57 ± 0.06- ($p < 10^{-16}$) fold between immortalized and transformed

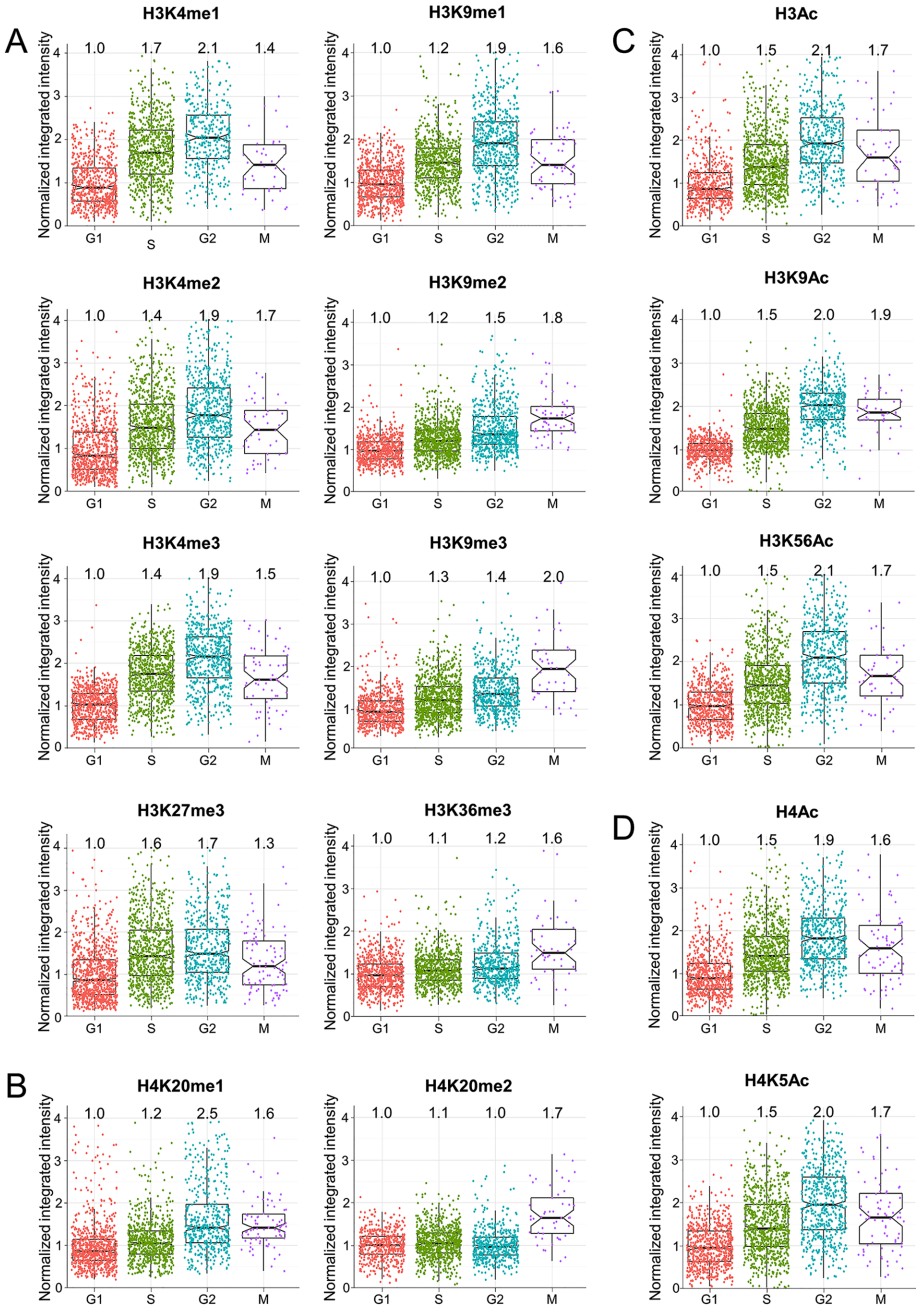

FIGURE 4: Single-cell levels of histone H3 and H4 methylation and acetylation during the cell cycle. Each dot represents the level of the histone H3 or H4 (A, B) methylation or (C, D) acetylation in a single cell. In box plots, the line corresponds to the median, notches represent the estimated 95% CI for the median, the lower and upper hinges of the box plot indicate the 25th and 75th percentiles, respectively, and the whiskers correspond to ± 1.5 × IQR of the hinge, where IQR is the interquartile range or distance between the first and third quartiles. The numbers above the box plots represent the means fold change compared with G1 levels. Each graph represents the results of two technical replicates.

cells in G1, S, G2, and M phases, respectively (Figures 5A and 6B). The same observation was made in HDFs from another individual (AG04551; see *Materials and Methods*; Supplemental Figure S10A).

We observed a statistically significant decrease of 0.5 ± 0.04- ($p < 10^{-16}$) and 0.5 ± 0.17- ($p < 10^{-16}$) fold in the level of H4K20me2 normalized to H4 between primary and transformed cells, as well as a decrease of 0.4 ± 0.05- ($p < 10^{-16}$) and 0.5 ± 0.12- ($p < 10^{-16}$) fold between immortalized and transformed cells in G1 and M phases, respectively (Figures 5B and 6C). All results were confirmed in three independent experiments, and similar results were observed in HDFs from three individuals (Figure 5B and Supplemental Figures S9B and S10B).

HiHiMap was also able to detect and display differences in the behavior of individual histones and histone modifications across the cell cycle (Figure 7). For this analysis, values were normalized to the G1 values for each modification. The values of 21 histone variants and modifications across the cell cycle of primary, immortalized, and transformed cells are represented as a heat map in Figure 7. For example, the level of H4K20me2 normalized to H4 was relatively stable during the cell cycle in transformed cells, with 0.86 ± 0.04-, 0.96 ± 0.03-, and 1.27 ± 0.03-fold changes in S, G2, and M phases compared with G1 ($p = 8.3 \times 10^{-5}$, 2.17×10^{-1}, and 2.97×10^{-13}). However, a decrease of 0.47 ± 0.04- and 0.48 ± 0.04-fold in S and G2 phases followed by an increase of 1.3 ± 0.01-fold in mitosis compared with G1 were observed in primary cells ($p < 10^{-16}$ for all S vs. G1, G2 vs. G1, and M vs. G1 comparisons). A decrease of 0.57 ± 0.03- and 0.55 ± 0.04-fold for H4K20me2 in S and G2 phases followed by a 1.17 ± 0.02-fold increase in M were also observed in immortalized cells ($p = 1.42 \times 10^{-15}$, 7.4×10^{-14}, and 1.87×10^{-3}; Figures 6C and 7B). Similar results were observed in HDFs of two additional individuals (Supplemental Figures 11B and 12B).

Similarly, the level of H2AX is stable during the cell cycle in transformed cells, with a 0.93 ± 0.05-, 0.82 ± 0.04-, and 0.86 ± 0.13-fold change in S, G2, and M phases compared with G1 ($p = 2.29 \times 10^{-2}$ in S, $p = 3.7 \times 10^{-15}$ in G2, and $p = 2.2 \times 10^{-6}$ in M) but fluctuates by 1.31 ± 0.02- ($p = 1.04 \times 10^{-6}$) and 1.42 ± 0.02- (3.3×10^{-6}) fold in S, by 1.19 ± 0.02- ($p = 5.6 \times 10^{-6}$) and 1.2 ± 0.025-fold in G2 ($p = 8.4 \times 10^{-5}$), and by 0.66 ± 0.05- ($p = 2.8 \times 10^{-33}$) and 0.7 ± 0.05- ($p = 1.1 \times 10^{-14}$) fold in M phase compared with G1, respectively, in primary and immortalized cells (Figures 6C and 7C). These results point to considerable effects on histones and histone modifications during oncogenic transformation.

DISCUSSION

We developed an imaging-based method, HiHiMap, to quickly and quantitatively measure histone and histone PTM levels throughout the cell cycle at the single-cell level using high-throughput microscopy. For validation, we showed that HiHiMap is able to detect several expected changes in histones and histone modifications through the cell cycle, demonstrated proof of principle by measurement of a comprehensive set of 25 histones and histone

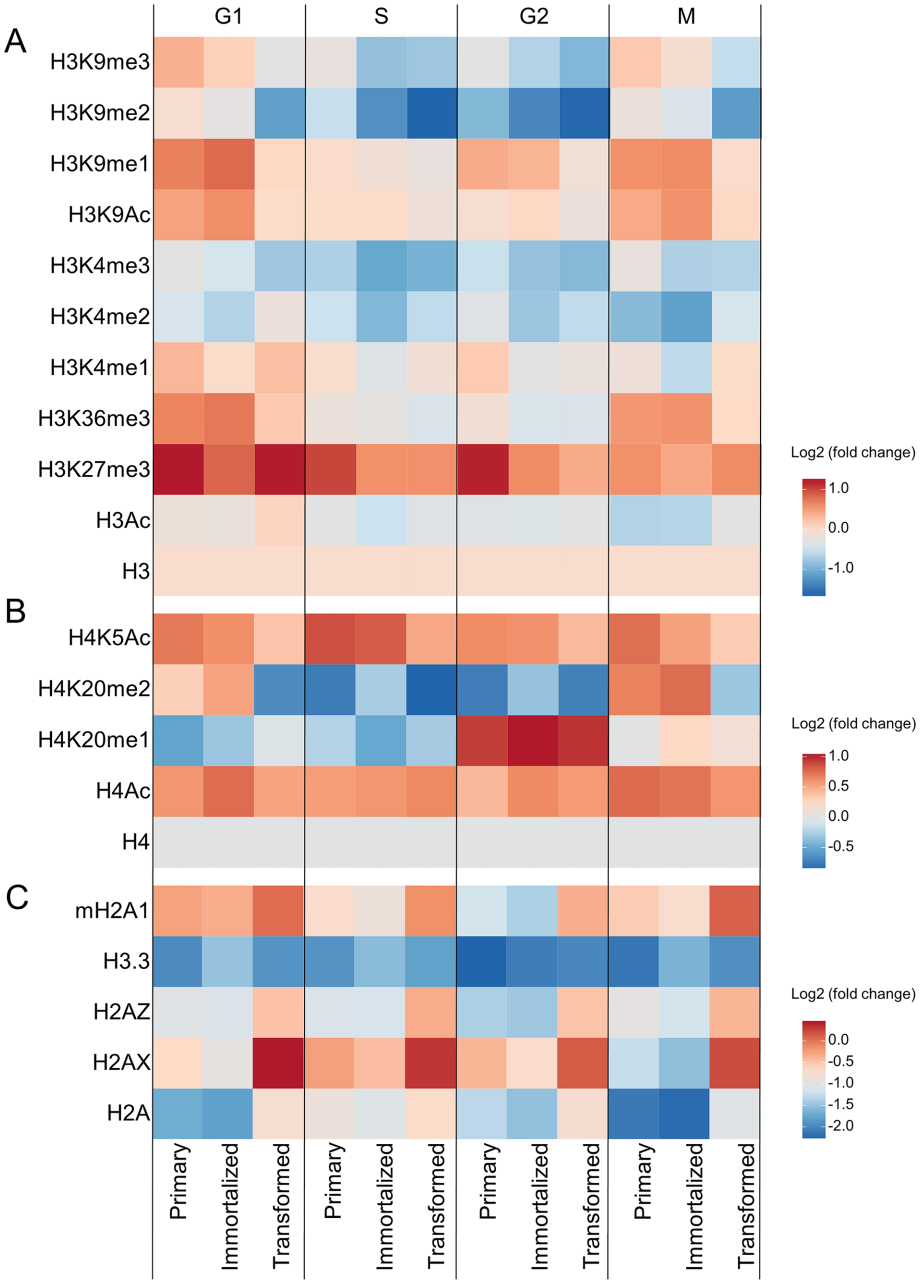

FIGURE 5: Heat maps of changes in histone and PTM levels during carcinogenesis at each cell cycle phase. Fold changes in (A) H3 modification levels normalized to DNA amount and H3 levels, (B) H4 modification levels normalized to DNA amount and H4 levels, and (C) histone and histone variant levels normalized to DNA amount in primary human skin fibroblasts and their hTERT-immortalized and transformed counterparts in AG06310 cells in G1, S, G2, and M phases. Each heat map represents the results of two technical replicates.

modifications, and showed its ability for discovery by identification of changes in a wide range of histone modifications during oncogenic transformation

HiHiMap overcomes several limitations of traditional methods, such as Western blotting and SILAC-MS, to determine histones and histone modification levels across the cell cycle. HiHiMap does not require any cell synchronization, which often results in impure populations and may affect histone and histone PTM levels, nor does it necessitate in vivo protein labeling steps, which may interfere with protein function. HiHiMap also provides practical advantages in that it is a rapid and easy method to study a wide range of histones and histone modifications in a fully automated manner, enabling comprehensive analysis of a large number of histones and histone modifications in a single experiment. HiHiMap is a rapid method, requiring only 48 h between seeding of cells and analysis of the results. If cells are seeded and cultured in 384-well plates overnight, the fixation and staining steps can be performed the next day, the image acquisition overnight, and the image analysis on the second day (see *Materials and Methods*), further accelerating the method. In addition, considerably lower numbers of cells are needed for HiHiMap (3000–5000 cells/sample per histone or histone PTM) than for the other methods (typically 10^6 cells/sample). This is particularly advantageous when working with patient samples. For example, to study 21 histones and histone PTMs during oncogenic transformation, with the controls, a total of only ~150,000 cells/sample was needed.

HiHiMap allows comparing histone and PTM levels between samples with different cell cycle distributions in an accurate manner by comparing the levels between samples at each cell cycle phase. Numerous studies aimed at investigating changes in histone PTM levels during biological processes such as cancer and differentiation (Pogribny *et al.*, 2006; Sridharan *et al.*, 2013; Zhao *et al.*, 2016; Piunti *et al.*, 2017) analyze differences in histones and histone modification levels in bulk, most often by Western blotting, enzyme-linked immunosorbent assay (ELISA; Ugarte *et al.*, 2015), or Nu-ELISA (Dai *et al.*, 2013), and normalize histone PTM levels to a core histone level. Mass spectrometry methods (Sridharan *et al.*, 2013; Piunti *et al.*, 2017) routinely calculate the percentage of the peptide carrying the PTM of interest to the sum of all the isoforms of that peptide. These normalization approaches correct the variations in the PTM levels relative to the variations due to differences in core histone levels. However, as our observations show, histone PTM levels during the cell cycle vary differently than the core histone levels (Figures 3–5). It is thus imperative to normalize at each cell cycle phase and compare histone PTM levels between samples at similar cell cycle phases, especially if the samples display different cell cycle distributions. For example, differences in cell cycle distribution between differentiated cells and stem cells are well documented, with stem cells showing a shorter G1 phase and more cells in S phase (Fan *et al.*, 2011; Hindley and Philpott, 2013). HiHiMap enables detection of differences in the cell cycle regulation of histone modification levels during the cell cycle in different cell types. As such, HiHiMap, in contrast to bulk methods, is suitable to study with high accuracy the differences in histones and PTM levels between samples by distinguishing the contribution due to different cell cycle distribution versus potentially

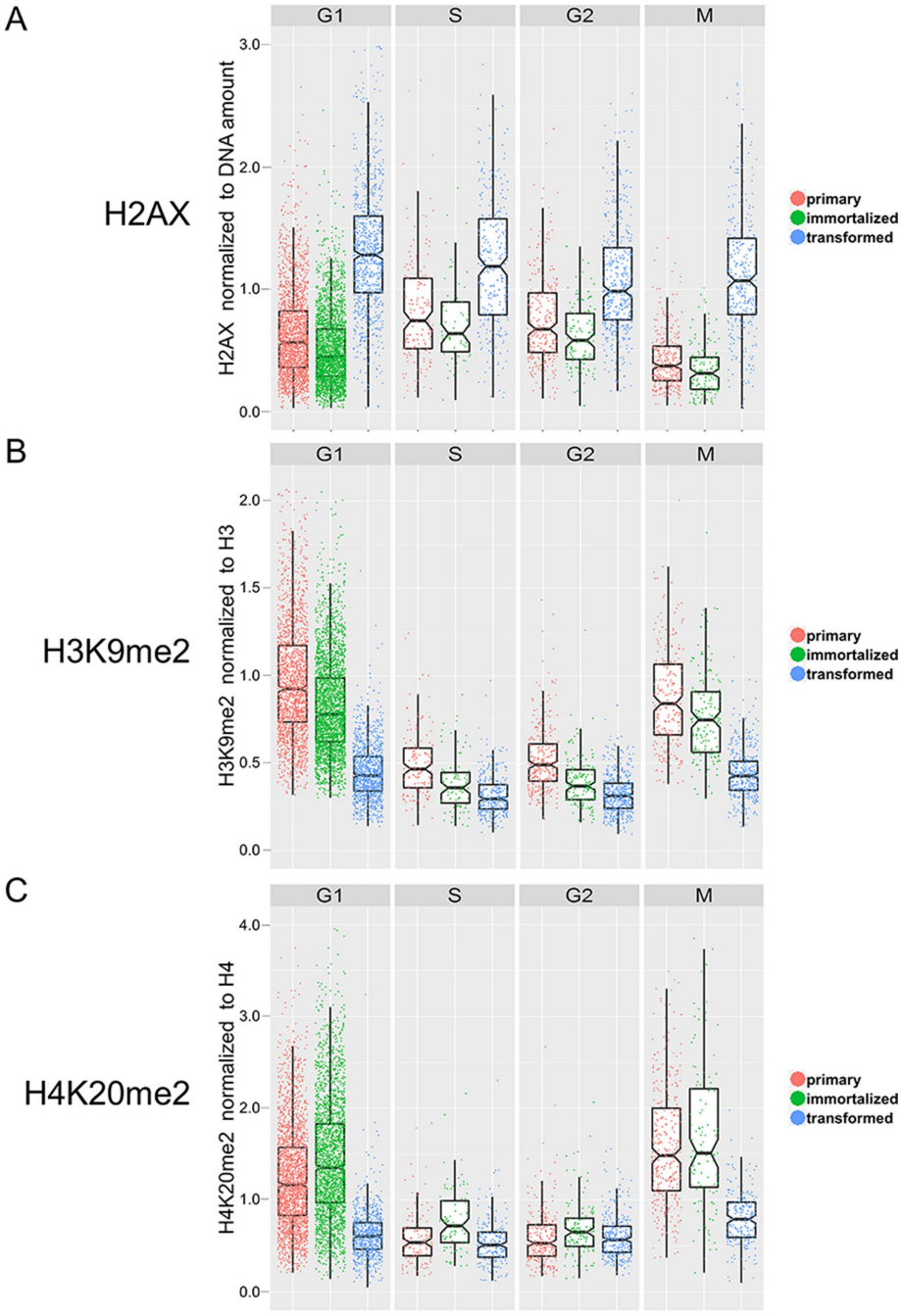

FIGURE 6: Relative single-cell levels of histones and PTM at each cell cycle phase. Single-cell intensity levels of (A) histone H2AX normalized to DNA amount, (B) H3K9me2 normalized to H3 levels, and (C) H4K20me2 normalized to H4 levels in primary, immortalized, and transformed cells in AG06310 cells in G1, S, G2, and M phases. Each dot represents the level of the histone or histone modification of interest in a single cell. In box plots, the line corresponds to the median, notches represent the estimated 95% CI for the median, the lower and upper hinges of the box plot indicate the 25th and 75th percentiles, respectively, and the whiskers correspond to ± 1.5 × IQR of the hinge, where IQR is the interquartile range or distance between the first and third quartiles. Each graph represents the results of two technical replicates.

distinct cell cycle regulation of histone PTM levels. The high sensitivity of HiHiMap with regard to cell cycle distributions is of particular importance because changes in histones and PTM levels are often less than twofold.

Furthermore, HiHiMap allows visualization of the distribution of histones and PTM in individual nuclei, which enables correlations of histone and histone modification levels relative to cellular features, for example, the formation of senescence-associated heterochromatin foci in individual cells in the population (Narita *et al.*, 2003; Zhang *et al.*, 2005) or, as shown here, relative to the ploidy level of individual cells, a feature important in the analysis of cancer samples (Torres *et al.*, 2008). Most importantly, HiHiMap is a single-cell analysis method and, in contrast to biochemical methods, which use bulk analysis and generate population averages, it measures histones and histone PTM in single cells whose position in the cell cycle has been determined. The method thus allows the study of the behavior of subpopulations of cells and of the variability within a population. For example, for most histones and histone PTMs, we find much greater variability in the single-cell distribution of levels in transformed cells than within the primary or immortalized populations (Figure 6A). In addition, pooling of single-cell data across the typically 1000–2000 analyzed cells also allows derivation of population averages, making the data comparable to biochemical data sets. Of note, HiHiMap can be adapted with minor modifications to IF staining, image acquisition, and analysis to the simultaneous detection of additional cellular markers, for example, to distinguish subpopulation of cells. Similarly, HiHiMap has the potential to be adapted to measure several histone marks in the same cell using cyclic immunofluorescence, a procedure involving repeated rounds of fluorescence staining and fluorophore inactivation (Lin *et al.*, 2015, 2016). Such a multiplexing approach would allow correlation of the intensity levels of different histone PTMs to test whether correlations are lost during biological processes such as cancer. HiHiMap can also be applied to nonadherent cells or primary cells by using poly-D-lysine–coated plates and a centrifugation step (Hakim *et al.*, 2012). Finally, this approach will also have utility in quickly verifying antibodies by comparing the variations in the intensity levels through the cell cycle using different antibodies against the same histone or PTM of interest (Supplemental Figure S2).

A limitation of HiHiMap is that it cannot distinguish between free and bound histones in the nucleus or between the same modifications on multiple isoforms of core histones. In addition, HiHiMap also does not distinguish preexisting from newly deposited histones or histone modifications after DNA replication. Furthermore, the method requires use of antibodies for detection. However, the abundance of well-characterized antibodies against a wide array of histones and histone modifications in various species lessens this concern. Furthermore, the highly compacted

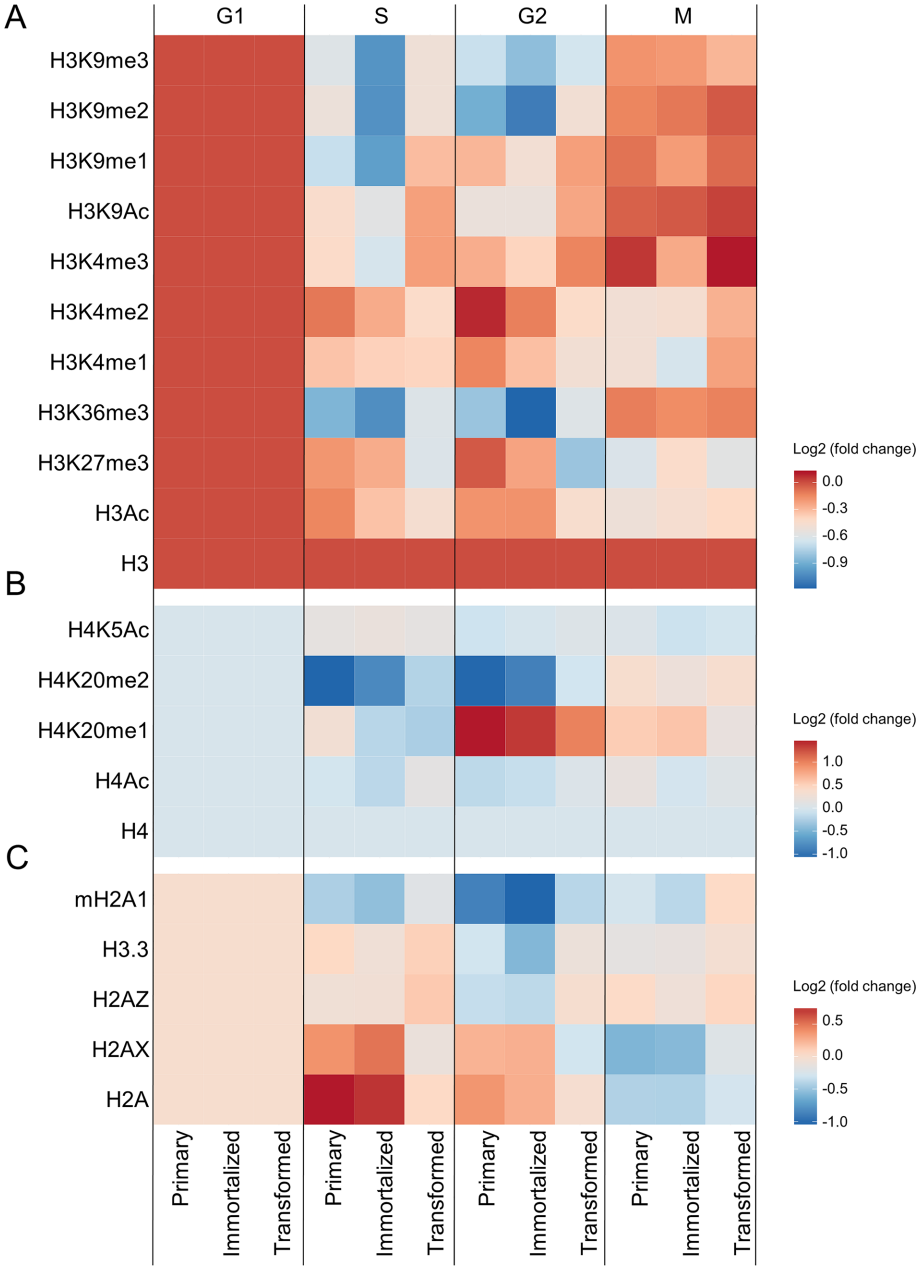

FIGURE 7: Heat map plots of changes in histone and histone PTM levels during the cell cycle. Fold changes in (A) H3 modification levels normalized to DNA amount and H3 levels, (B) H4 modification levels normalized to H4 levels, and (C) histone and histone variant levels of primary, immortalized, and transformed cells after normalization to their respective level in AG06310 cells in G1, S, G2, and M phases. Each heat map represents the results of two technical replicates.

chromatin in mitosis may interfere with the binding of the antibodies and with the automated nuclei detection, which explains the lower level of core histones in M phase than in G2 (Figure 3A). Finally, Hi-HiMap, in contrast to mass spectrometry, is not able to determine whether two histone marks whose intensity levels correlate in fact co-occur on the same nucleosome or the same histone molecule nor does it, in contrast to combinatorial indexed chromatin immunoprecipitation (iChIP; Sadeh *et al.*, 2016), co-ChIP (Weiner *et al.*, 2016) sequencing, or re-ChIP-sequencing (Kinkley *et al.*, 2016) methods, provide information on the genomic location at which these interactions occur.

As proof of principle for its application as a discovery tool, we investigated global changes of histones and histone PTM levels during oncogenic transformation. In an established cell-based transformation model, we find a number of changes in histones and histone modifications over the course of oncogenic transformation, pointing to potential biological mechanisms. Of significance, we find reduction of H3K9me2 in the transformed cells compared with their primary and immortalized counterparts. This PTM is known to mark condensed heterochromatin and thus gene inactivation (Lehnertz *et al.*, 2003; Barski *et al.*, 2007; Towbin *et al.*, 2012) and was recently shown to be decreased in an in vitro tumor transformation model of human primary mammary cells and in breast cancer tissues (Zhao *et al.*, 2016). Similarly, global levels of H3K9me2 are significantly lower in bladder cancer than in normal urothelial tissue, and levels in muscle invasive bladder cancer are lower compared with nonmuscle invasive bladder cancer (Ellinger *et al.*, 2014). In prostate (Ellinger *et al.*, 2010) and kidney (Seligson *et al.*, 2009) cancers, as well as in clear cell renal cell carcinoma (Xing and He, 2016), lower levels of H3K9me2 have been associated with disease outcome and predict poor prognosis. We also found a decrease in H4K20me2, the most abundant methylation mark on histone H4 in proliferating cells (Pesavento *et al.*, 2008), which has been linked to DNA damage and DNA repair (Botuyan *et al.*, 2006) and genomic instability (Jorgensen *et al.*, 2013). In agreement with our results, hypomethylation of H4K20 has been shown in metastatic and castration-resistant prostate cancer compared with normal prostate tissue (Behbahani *et al.*, 2012) and in several other cancers, including bladder (Schneider *et al.*, 2011) and liver tumors (Pogribny *et al.*, 2006). Finally, we found increased levels of H2AX in transformed cells compared with their primary and immortalized counterparts. The histone variant H2AX has been implicated in tumor development by virtue of frequent mutations and deletions of chromosome region 11q23, which contains the H2AX gene, in a large number of human cancers, especially hematopoietic malignancies (Thirman *et al.*, 1993; Bassing *et al.*, 2003) and head and neck squamous cell carcinoma (Parikh *et al.*, 2007), and H2AX-knockout mice show increased genomic instability and a higher risk of developing cancers (Celeste *et al.*, 2002). In addition, phosphorylation of H2AX plays a key role in the DNA damage response (Rogakou *et al.*, 1998), and its levels are increased in many cancer cells (Banath *et al.*, 2004; Sedelnikova and Bonner, 2006; Yu *et al.*, 2006; Nagelkerke *et al.*, 2011).

We have developed a fast, versatile, and scalable method to measure in individual cells the levels of histones and histone PTMs

throughout the cell cycle. We validated the method and applied it to identify changes in histones and histone modifications during oncogenic transformation. We anticipate that HiHiMap will be a useful tool to study the regulation of histone and histone PTM levels through the cell cycle in a wide range of physiological and pathological conditions.

MATERIALS AND METHODS

Cell culture

hTERT-immortalized human diploid fibroblasts (HDFs), CRL-1575, and primary HDFs from healthy Caucasian individuals (AG06310A, AG06289A, and AG04551A; Coriell Cell Repository) were cultured in MEM (Life Technologies) supplemented with 15% (vol/vol) fetal bovine serum (FBS; Atlanta Biologicals), 1% (vol/vol) penicillin/streptomycin (P/S), and 1% (vol/vol) L-glutamine (Life Technologies). TSA dissolved in dimethyl sulfoxide was purchased from Sigma-Aldrich.

Cell transformation

Immortalized and transformed human cell lines were generated as described (Hahn *et al.*, 1999) from HDFs. Recombinant retroviral vectors expressing human telomerase hTERT, SV40 early region (LT and ST antigens), and oncogenic H-RasV12 were introduced simultaneously to generate transformed cells. Retroviral vector supernatants were produced by cotransfecting 10-cm dishes of HEK293T cells (American Type Culture Collection) with each of the packaging plasmids pGAG-pol and pVSV-G and with pBABE-puro-hTERT, pBABE-zeo-large T genomic, or pBABE-neo-rasV12 (X-treme GENE HP DNA transfection reagent; Roche). The medium of 293T cells was changed 12 h after transfection, and 6 ml per 10-cm dish of fresh medium was added. Viral vector supernatants were harvested 24 h later and used to transduce HDFs with 5 µg/ml Polybrene. Typically, 30–60% transduction efficiency of the HDFs was achieved by using this protocol as measured by parallel transductions with a green fluorescent protein–expressing retroviral vector instead of the infection with hTERT-expressing retroviral construct. Then transduced cells were selected using puromycin (5 µg/ml), Zeocin (100 µg/ml), or neomycin (0.5 µg/ml) for 15 d to purify polyclonal-transduced populations. These immortalized and transformed cell lines were grown as described. All cells were grown at 37°C in 5% CO_2.

Western blot and real-time quantitative reverse transcriptase–PCR

Briefly, cells were lysed and DNA was sonicated. After determining protein concentration, 5 µg of total proteins was loaded on a NuPAGE Novex 4-12% Bis-Tris Protein Gel (ThermoFisher). After protein transfer on a polyvinylidene fluoride membrane (Immobilon P; 161-0737; Millipore), expression of SV40LT and H-Ras proteins was measured by incubation of this membrane with SV40LT antibody Ab101 (1:1000; 554149; BD Pharmingen) and pan-Ras antibody (final concentration 0.3 µg/ml; OP40; Calbiochem). Intensities of protein bands, revealed by chemiluminescent reagents, were measured using a ChemiDoc MP imaging system from Bio-Rad. The expression of pan-Ras and SV40LT was normalized to the endogenous expression of glyceraldehyde-3-phosphate dehydrogenase (GAPDH).

For real-time quantitative reverse transcriptase–PCR, total cellular RNA was isolated using the RNeasy kit according to the manufacturer's instructions (74136; Qiagen). The first-strand cDNA was synthesized from 0.5 µg of RNA using random primers and MultiScribe reverse transcriptase (from a High-Capacity cDNA Reverse Transcription kit; 4368813; Applied Biosystems). RNA concentration and purity were determined by ultraviolet (UV) spectrophotometry (NanoDrop). The primer pairs used were as follows: hTERT-F, 5′GAGCTGACGTGGAAGATGAG3′; hTERT-R, 5′CAGGATCTCCTCACGCAGAC3′; V12hRAS_4F, 5′GCAAGTGTGTGCTCTCCTGA3′; V12hRAS_4R, 5′CTGGCGAATTCCTACAGCTT3′; SV40_LT6_F, 5′TTGGAGGCCTAGGCTTTTG3′, and SV40_LT6_R, 5′CAGGCACTCCTTTCAAGACC3′; Scaffidi and Misteli, 2011). Each primer pair was designed to generate an amplicon across different exons to avoid genomic amplification. GAPDH was used as the reference gene for the normalization of results (GAPDH-R, 5′ACCCACTCCTCCACCTTTGA3′; GAPDH-F, 5′CTGTTGCTGTAGCCAAATTCGT3′). PCR was performed using iQ SYBR Green Supermix on a CFX96 real-time PCR system (Bio-Rad). A large amount of cDNA was prepared from the control cell line, 66^{+++} cells, a transformed human skin fibroblast cell line that forms colonies in soft agar and tumors in immunocompromised mice (Scaffidi and Misteli, 2011). The cDNA was diluted 10 times, aliquoted, and used as a calibrator. Serial dilutions of 66^{+++} cDNA were used to determine the PCR efficiency of each primer. For relative quantification and normalization, the comparative *Ct* (or Eff-DDC) method was used (Livak and Schmittgen, 2001).

Soft agar assay

Soft agar assays were performed in three-layer soft agar in six-well plates. A bottom layer of 0.6% Agar Noble (Lonza) in MEM was first placed onto 6-cm dishes. Five thousand immortalized or transformed HDFs per well were seeded in 0.45% top agar in MEM with FBS, P/S, and Fungizone (250 µg/ml). Fresh top agar was added after 1.5 wk, and, after 3 wk, colonies were stained overnight at 37°C with 3-(4,5-dimethylthiazol-2-yl)-2,5-diphenyltetrazolium bromide (Sigma-Aldrich) at a concentration of 10 mg/ml (1:100) in phosphate-buffered saline (PBS). Colonies were counted by using ImageJ software.

High-throughput microscopy

Cells were plated in 384-well CellCarrier plates (PerkinElmer, Waltham, MA) at a concentration of 60 cells/µl (3000 cells/well) and incubated for 24 h before IF staining. Cells were fixed in 4% PFA in PBS for 15 min, washed for 5 min three times with PBS, and permeabilized in 0.5% Triton X-100/PBS for 15 min at room temperature. Cells were then washed for 5 min three times with PBS, blocked for 20 min with 3% bovine serum albumin/PBS, and incubated with the indicated primary rabbit or mouse antibodies at the indicated concentrations (Supplemental Table S1) and anti–cyclin-A2 antibody (1:125; clone 6E6; ab16726; Abcam) for 30 min at room temperature and washed for 5 min three times with PBS before a 30-min incubation with appropriate anti-rabbit or anti-mouse secondary antibodies labeled with Alexa 488 (1:200; A11034) or Alexa 647 (1:200; A31571; Life Technologies). After three 5-min washes with PBS, DNA was counterstained with 10 µg/ml DAPI for 10 min at room temperature. Cells were left in 100 µl/well PBS and either immediately imaged or stored at 4°C in sealed plates until imaging. In all experiments, one histone or histone modification was detected per well using manual staining.

Image acquisition

Imaging was performed on an Opera QEHS high-content screening microscopy system (PerkinElmer) running the Opera 2.0.1 software using a 40× water immersion (numerical aperture [NA] 0.9) or a 20× water immersion (NA 0.7) objective lens and three 12-bit 1.3-megapixel charge-coupled device cameras with a pixel binning setting of 2, corresponding to a final pixel size of 323 nm for the 40× objective and 646 nm for the 20×. DAPI, Alexa 488, and Alexa 647 were

sequentially acquired in 150 (when using the 40× lens) or 50 (when using the 20× lens) randomly sampled fields per well using a UV polychrome box (wide field), a 488-nm laser (confocal), and a 640-nm laser (confocal). Typically, at least 3000 cells were imaged for each condition (~1500 cells/well and two wells per histone or PTM).

Automated image analysis

Acquired images were analyzed with Columbus 2.5 or 2.6 (PerkinElmer) software. Nuclei were segmented based on the DAPI channel. Nuclear debris and/or nuclear segmentation errors were eliminated by manually setting combined nuclear area and roundness filters. The resulting nucleus region of interest was then used as the search region to measure integrated and mean fluorescence intensities of DAPI, cyclin A, and histone or PTM of interest in the UV, Alexa 488, and Alexa 647 channels, respectively.

Single-cell image analysis results were exported as tab-separated text files and further analyzed with R statistical analysis software (https://cran.r-project.org/). Cell cycle phases G1, S, and G2/M were determined as described previously (Roukos *et al.*, 2015) using the DAPI intensity levels. In addition, we identified G2 cells by the marker protein cyclin A2.

Cell cycle profiling by imaging

For the high-throughput microscopy pipeline, a dedicated R script was generated. First, the cell cycle profiles for each well based on the integrated DAPI intensity were plotted, and, after a visualization of the range of G1 and G2 peak values in different wells, the positions of the peak maxima were calculated using a nonparametric mixed model estimation in the R mixtools package (Benaglia, 2009) or by manually determining the positions of the peaks when the model was unable to calculate them. The G1 peak value was set to 1 to define the same thresholds for G1, S, and G2/M phases in all samples (Supplemental Figure S1A). After plotting of a histogram for the cyclin A intensity values, the cyclin A threshold for all wells of a 384-well plate was manually defined based on the background staining in the wells incubated without cyclin A antibody but with the secondary antibodies. Then the cell cycle stage associated with each individual cell in the data set was determined based on both cyclin A and DAPI thresholds. Boxplots overlaid with dot plots of the integrated intensity of a histone or PTM at each cell cycle phase were created, and text files containing the geometric mean integrated intensity and mean fluorescence intensity for each histone and PTM studied at each cell cycle stage were generated.

To compare the levels of histones and histone PTMs in primary, immortalized, and transformed cells, several steps were added to the R script. To take into consideration the ploidy status of the transformed cells, the histone and histone PTM levels were normalized to the DAPI amount. For PTMs on H3 and H4, we normalized their levels to the mean of the level of the corresponding core histone as follows:

$$\frac{(\text{histone PTM/DNA})_i}{\frac{1}{n}\sum_{j=1}^{n}(\text{core histone/DNA})_j}$$

where n is the number of cells, i is the level of histone PTM normalized to the DNA amount in one single cell, j is the level of the core histone corresponding to the histone PTM normalized to the DNA amount in one single cell, and i and j correspond to cells in different wells.

The levels of core histones and histone PTMs were normalized to their respective DNA amounts.

To simplify the representation of the results, we show results for tetraploid cells, which is the major population of transformed cells. For example, the transformed cells of the AG06289 sample displayed a mixed population of diploid and tetraploid cells. The tetraploid cells represent the main population, and their histone and histone PTM levels are indicated in the graphs. Note that after normalization to the DNA amount, the results for the tetraploid and diploid cells gave similar results.

Cell cycle profiling by flow cytometry

Cell cycle distribution was assessed by measuring the DNA content of a suspension of fresh nuclei by flow cytometric analysis after propidium iodide (PI) staining. Cells from one 60–80% confluent 10-cm dish were washed with PBS. The supernatant was discarded, and cells were resuspended in 50 µl of PBS and fixed with 450 µl of 70% ethanol for 30 min at 4°C and then stored at –20°C. After ethanol elimination, cells were washed twice with PBS and labeled with PI (P4864; Sigma-Aldrich) in the presence of RNase A (100 mg/ml; Sigma-Aldrich), scanned by flow cytometry using a FACSCalibur, and analyzed using BD Cell Quest Pro software.

Statistical analysis

Bar chart results are represented as mean ± 1 SD of a minimum of three biological replicates.

For comparisons of histone and histone PTM levels between groups, results are represented as notched box plots using R (R Core Team, 2015) and the ggplot2 package (Wickham, 2009). Box plot notches indicate the estimated 95% confidence interval (CI) for the estimated median value, calculated as $\pm 1.58 \times \text{IQR}/\sqrt{n}$, where IQR is the interquartile range or distance between the first and third quartiles, and n is the number of cells (McGill *et al.*, 1978). The lower and upper hinges of the box plots correspond to the first and third quartiles (25th and 75th percentiles, respectively). The upper and lower whiskers extend from the hinge to $\pm 1.5 \times$ IQR of the hinge.

The Student's t test was used for all pairwise comparisons, and p values were adjusted using the Benjamini–Hochberg multiple test correction. $p < 0.05$ was considered statistically significant. All statistical analyses were performed using R statistical analysis software.

To determine the minimal sample size, two randomly selected samples from a population of G1 cells from a single well were randomly subsampled from a single population of G1 cells imaged in a single well, and their histone levels were compared using the two-sample KS test. The subsampling simulation was repeated 10,000 times for each indicated cell number, and the fraction of trials generating $p < 0.005$ was calculated. We find that to generate $p < 0.005$ in >95% of the cases, the size of the sample must be at least 230 cells.

ACKNOWLEDGMENTS

We thank Sigal Shachar for technical help with the Opera and members of the Misteli laboratory for helpful discussions and comments. This research was supported by the Intramural Research Program of the National Institutes of Health, National Cancer Institute, and Center for Cancer Research.

REFERENCES

Alabert C, Barth TK, Reveron-Gomez N, Sidoli S, Schmidt A, Jensen ON, Imhof A, Groth A (2015). Two distinct modes for propagation of histone PTMs across the cell cycle. Genes Dev 29, 585–590.

Almouzni G, Cedar H (2016). Maintenance of epigenetic information. Cold Spring Harb Perspect Biol 8, a019372.

Banath JP, Macphail SH, Olive PL (2004). Radiation sensitivity, H2AX phosphorylation, and kinetics of repair of DNA strand breaks in irradiated cervical cancer cell lines. Cancer Res 64, 7144–7149.

Barski A, Cuddapah S, Cui K, Roh TY, Schones DE, Wang Z, Wei G, Chepelev I, Zhao K (2007). High-resolution profiling of histone methylations in the human genome. Cell 129, 823–837.
Bassing CH, Suh H, Ferguson DO, Chua KF, Manis J, Eckersdorff M, Gleason M, Bronson R, Lee C, Alt FW (2003). Histone H2AX: a dosage-dependent suppressor of oncogenic translocations and tumors. Cell 114, 359–370.
Beck DB, Burton A, Oda H, Ziegler-Birling C, Torres-Padilla ME, Reinberg D (2012a). The role of PR-Set7 in replication licensing depends on Suv4-20h. Genes Dev 26, 2580–2589.
Beck DB, Oda H, Shen SS, Reinberg D (2012b). PR-Set7 and H4K20me1: at the crossroads of genome integrity, cell cycle, chromosome condensation, and transcription. Genes Dev 26, 325–337.
Behbahani TE, Kahl P, von der Gathen J, Heukamp LC, Baumann C, Gutgemann I, Walter B, Hofstadter F, Bastian PJ, von Ruecker A, *et al.* (2012). Alterations of global histone H4K20 methylation during prostate carcinogenesis. BMC Urol 12, 5.
Benaglia T, Chauveau D, Hunter DR, Young DS (2009). Mixtools: an R package for analyzing finite mixture models. J Stat Softw 32, 1–29.
Botuyan MV, Lee J, Ward IM, Kim JE, Thompson JR, Chen J, Mer G (2006). Structural basis for the methylation state-specific recognition of histone H4-K20 by 53BP1 and Crb2 in DNA repair. Cell 127, 1361–1373.
Budhavarapu VN, Chavez M, Tyler JK (2013). How is epigenetic information maintained through DNA replication? Epigenetics Chromatin 6, 32.
Celeste A, Petersen S, Romanienko PJ, Fernandez-Capetillo O, Chen HT, Sedelnikova OA, Reina-San-Martin B, Coppola V, Meffre E, Difilippantonio MJ, *et al.* (2002). Genomic instability in mice lacking histone H2AX. Science 296, 922–927.
Chantalat S, Depaux A, Hery P, Barral S, Thuret JY, Dimitrov S, Gerard M (2011). Histone H3 trimethylation at lysine 36 is associated with constitutive and facultative heterochromatin. Genome Res 21, 1426–1437.
Dai B, Giardina C, Rasmussen TP (2013). Quantitation of nucleosome acetylation and other histone posttranslational modifications using microscale NU-ELISA. Methods Mol Biol 981, 167–176.
Egelhofer TA, Minoda A, Klugman S, Lee K, Kolasinska-Zwierz P, Alekseyenko AA, Cheung MS, Day DS, Gadel S, Gorchakov AA, *et al.* (2011). An assessment of histone-modification antibody quality. Nat Struct Mol Biol 18, 91–93.
Elenbaas B, Spirio L, Koerner F, Fleming MD, Zimonjic DB, Donaher JL, Popescu NC, Hahn WC, Weinberg RA (2001). Human breast cancer cells generated by oncogenic transformation of primary mammary epithelial cells. Genes Dev 15, 50–65.
Ellinger J, Bachmann A, Goke F, Behbahani TE, Baumann C, Heukamp LC, Rogenhofer S, Muller SC (2014). Alterations of global histone H3K9 and H3K27 methylation levels in bladder cancer. Urol Int 93, 113–118.
Ellinger J, Kahl P, von der Gathen J, Rogenhofer S, Heukamp LC, Gutgemann I, Walter B, Hofstadter F, Buttner R, Muller SC, *et al.* (2010). Global levels of histone modifications predict prostate cancer recurrence. Prostate 70, 61–69.
Elsheikh SE, Green AR, Rakha EA, Powe DG, Ahmed RA, Collins HM, Soria D, Garibaldi JM, Paish CE, Ammar AA, *et al.* (2009). Global histone modifications in breast cancer correlate with tumor phenotypes, prognostic factors, and patient outcome. Cancer Res 69, 3802–3809.
Fan J, Robert C, Jang YY, Liu H, Sharkis S, Baylin SB, Rassool FV (2011). Human induced pluripotent cells resemble embryonic stem cells demonstrating enhanced levels of DNA repair and efficacy of nonhomologous end-joining. Mutat Res 713, 8–17.
Fernandez P, Scaffidi P, Markert E, Lee JH, Rane S, Misteli T (2014). Transformation resistance in a premature aging disorder identifies a tumor-protective function of BRD4. Cell Rep 9, 248–260.
Hahn WC, Counter CM, Lundberg AS, Beijersbergen RL, Brooks MW, Weinberg RA (1999). Creation of human tumour cells with defined genetic elements. Nature 400, 464–468.
Hahn WC, Dessain SK, Brooks MW, King JE, Elenbaas B, Sabatini DM, DeCaprio JA, Weinberg RA (2002). Enumeration of the simian virus 40 early region elements necessary for human cell transformation. Mol Cell Biol 22, 2111–2123.
Hakim O, Resch W, Yamane A, Klein I, Kieffer-Kwon KR, Jankovic M, Oliveira T, Bothmer A, Voss TC, Ansarah-Sobrinho C, *et al.* (2012). DNA damage defines sites of recurrent chromosomal translocations in B lymphocytes. Nature 484, 69–74.
Hindley C, Philpott A (2013). The cell cycle and pluripotency. Biochem J 451, 135–143.
House NC, Koch MR, Freudenreich CH (2014). Chromatin modifications and DNA repair: beyond double-strand breaks. Front Genet 5, 296.
Jenuwein T, Allis CD (2001). Translating the histone code. Science 293, 1074–1080.
Jorgensen S, Schotta G, Sorensen CS (2013). Histone H4 lysine 20 methylation: key player in epigenetic regulation of genomic integrity. Nucleic Acids Res 41, 2797–2806.
Kinkley S, Helmuth J, Polansky JK, Dunkel I, Gasparoni G, Frohler S, Chen W, Walter J, Hamann A, Chung HR (2016). reChIP-seq reveals widespread bivalency of H3K4me3 and H3K27me3 in CD4(+) memory T cells. Nat Commun 7, 12514.
Kolasinska-Zwierz P, Down T, Latorre I, Liu T, Liu XS, Ahringer J (2009). Differential chromatin marking of introns and expressed exons by H3K36me3. Nat Genet 41, 376–381.
Kornberg RD, Lorch Y (1999). Twenty-five years of the nucleosome, fundamental particle of the eukaryote chromosome. Cell 98, 285–294.
Lehnertz B, Ueda Y, Derijck AA, Braunschweig U, Perez-Burgos L, Kubicek S, Chen T, Li E, Jenuwein T, Peters AH (2003). Suv39h-mediated histone H3 lysine 9 methylation directs DNA methylation to major satellite repeats at pericentric heterochromatin. Curr Biol 13, 1192–1200.
Lin JR, Fallahi-Sichani M, Chen JY, Sorger PK (2016). Cyclic immunofluorescence (CycIF), a highly multiplexed method for single-cell imaging. Curr Protoc Chem Biol 8, 251–264.
Lin JR, Fallahi-Sichani M, Sorger PK (2015). Highly multiplexed imaging of single cells using a high-throughput cyclic immunofluorescence method. Nat Commun 6, 8390.
Livak KJ, Schmittgen TD (2001). Analysis of relative gene expression data using real-time quantitative PCR and the 2(-Delta Delta C(T)) method. Methods 25, 402–408.
Loyola A, Bonaldi T, Roche D, Imhof A, Almouzni G (2006). PTMs on H3 variants before chromatin assembly potentiate their final epigenetic state. Mol Cell 24, 309–316.
Mannironi C, Bonner WM, Hatch CL (1989). H2A.X. a histone isoprotein with a conserved C-terminal sequence, is encoded by a novel mRNA with both DNA replication type and polyA 3′ processing signals. Nucleic Acids Res 17, 9113–9126.
Marzluff WF, Duronio RJ (2002). Histone mRNA expression: multiple levels of cell cycle regulation and important developmental consequences. Curr Opin Cell Biol 14, 692–699.
Marzluff WF, Wagner EJ, Duronio RJ (2008). Metabolism and regulation of canonical histone mRNAs: life without a poly(A) tail. Nat Rev Genet 9, 843–854.
McGill R, Tukey JW, Larsen WA (1978). Variations of box plots. Am Statistician 32, 12–16.
Nagelkerke A, van Kuijk SJ, Sweep FC, Nagtegaal ID, Hoogerbrugge N, Martens JW, Timmermans MA, van Laarhoven HW, Bussink J, Span PN (2011). Constitutive expression of gamma-H2AX has prognostic relevance in triple negative breast cancer. Radiother Oncol 101, 39–45.
Narita M, Nunez S, Heard E, Narita M, Lin AW, Hearn SA, Spector DL, Hannon GJ, Lowe SW (2003). Rb-mediated heterochromatin formation and silencing of E2F target genes during cellular senescence. Cell 113, 703–716.
Nelson DM, Ye X, Hall C, Santos H, Ma T, Kao GD, Yen TJ, Harper JW, Adams PD (2002). Coupling of DNA synthesis and histone synthesis in S phase independent of cyclin/cdk2 activity. Mol Cell Biol 22, 7459–7472.
Noma K, Allis CD, Grewal SI (2001). Transitions in distinct histone H3 methylation patterns at the heterochromatin domain boundaries. Science 293, 1150–1155.
Ong SE, Blagoev B, Kratchmarova I, Kristensen DB, Steen H, Pandey A, Mann M (2002). Stable isotope labeling by amino acids in cell culture, SILAC, as a simple and accurate approach to expression proteomics. Mol Cell Proteomics 1, 376–386.
Osley MA (1991). The regulation of histone synthesis in the cell cycle. Annu Rev Biochem 60, 827–861.
Pagano M, Pepperkok R, Verde F, Ansorge W, Draetta G (1992). Cyclin A is required at two points in the human cell cycle. EMBO J 11, 961–971.
Parikh RA, White JS, Huang X, Schoppy DW, Baysal BE, Baskaran R, Bakkenist CJ, Saunders WS, Hsu LC, Romkes M, Gollin SM (2007). Loss of distal 11q is associated with DNA repair deficiency and reduced sensitivity to ionizing radiation in head and neck squamous cell carcinoma. Genes Chromosomes Cancer 46, 761–775.
Pesavento JJ, Yang H, Kelleher NL, Mizzen CA (2008). Certain and progressive methylation of histone H4 at lysine 20 during the cell cycle. Mol Cell Biol 28, 468–486.

Piunti A, Hashizume R, Morgan MA, Bartom ET, Horbinski CM, Marshall SA, Rendleman EJ, Ma Q, Takahashi YH, Woodfin AR, *et al.* (2017). Therapeutic targeting of polycomb and BET bromodomain proteins in diffuse intrinsic pontine gliomas. Nat Med 23, 493–500.

Pogribny IP, Ross SA, Tryndyak VP, Pogribna M, Poirier LA, Karpinets TV (2006). Histone H3 lysine 9 and H4 lysine 20 trimethylation and the expression of Suv4-20h2 and Suv-39h1 histone methyltransferases in hepatocarcinogenesis induced by methyl deficiency in rats. Carcinogenesis 27, 1180–1186.

Polo SE, Almouzni G (2015). Chromatin dynamics after DNA damage: The legacy of the access-repair-restore model. DNA Repair (Amst) 36, 114–121.

R Core Team (2015). R: A Language and Environment for Statistical Computing, Vienna: R Foundation for Statistical Computing. Available at https://www.r-project.org (accessed 11 July 2017).

Rogakou EP, Pilch DR, Orr AH, Ivanova VS, Bonner WM (1998). DNA double-stranded breaks induce histone H2AX phosphorylation on serine 139. J Biol Chem 273, 5858–5868.

Rothbart SB, Strahl BD (2014). Interpreting the language of histone and DNA modifications. Biochim Biophys Acta 1839, 627–643.

Roukos V, Pegoraro G, Voss TC, Misteli T (2015). Cell cycle staging of individual cells by fluorescence microscopy. Nat Protoc 10, 334–348.

Sadeh R, Launer-Wachs R, Wandel H, Rahat A, Friedman N (2016). Elucidating combinatorial chromatin states at single-nucleosome resolution. Mol Cell 63, 1080–1088.

Sawicka A, Seiser C (2012). Histone H3 phosphorylation—a versatile chromatin modification for different occasions. Biochimie 94, 2193–2201.

Scaffidi P, Misteli T (2011). In vitro generation of human cells with cancer stem cell properties. Nat Cell Biol 13, 1051–1061.

Scharf AN, Barth TK, Imhof A (2009). Establishment of histone modifications after chromatin assembly. Nucleic Acids Res 37, 5032–5040.

Schlesinger Y, Straussman R, Keshet I, Farkash S, Hecht M, Zimmerman J, Eden E, Yakhini Z, Ben-Shushan E, Reubinoff BE, *et al.* (2007). Polycomb-mediated methylation on Lys27 of histone H3 pre-marks genes for de novo methylation in cancer. Nat Genet 39, 232–236.

Schneider AC, Heukamp LC, Rogenhofer S, Fechner G, Bastian PJ, von Ruecker A, Muller SC, Ellinger J (2011). Global histone H4K20 trimethylation predicts cancer-specific survival in patients with muscle-invasive bladder cancer. BJU Int 108, E290–E296.

Sedelnikova OA, Bonner WM (2006). GammaH2AX in cancer cells: a potential biomarker for cancer diagnostics, prediction and recurrence. Cell Cycle 5, 2909–2913.

Seligson DB, Horvath S, McBrian MA, Mah V, Yu H, Tze S, Wang Q, Chia D, Goodglick L, Kurdistani SK (2009). Global levels of histone modifications predict prognosis in different cancers. Am J Pathol 174, 1619–1628.

Seligson DB, Horvath S, Shi T, Yu H, Tze S, Grunstein M, Kurdistani SK (2005). Global histone modification patterns predict risk of prostate cancer recurrence. Nature 435, 1262–1266.

Sharma S, Kelly TK, Jones PA (2010). Epigenetics in cancer. Carcinogenesis 31, 27–36.

Sridharan R, Gonzales-Cope M, Chronis C, Bonora G, McKee R, Huang C, Patel S, Lopez D, Mishra N, Pellegrini M, *et al.* (2013). Proteomic and genomic approaches reveal critical functions of H3K9 methylation and heterochromatin protein-1gamma in reprogramming to pluripotency. Nat Cell Biol 15, 872–882.

Sweet SM, Li M, Thomas PM, Durbin KR, Kelleher NL (2010). Kinetics of re-establishing H3K79 methylation marks in global human chromatin. J Biol Chem 285, 32778–32786.

Swygert SG, Peterson CL (2014). Chromatin dynamics: interplay between remodeling enzymes and histone modifications. Biochim Biophys Acta 1839, 728–736.

Talbert PB, Henikoff S (2010). Histone variants–ancient wrap artists of the epigenome. Nat Rev Mol Cell Biol 11, 264–275.

Tan M, Luo H, Lee S, Jin F, Yang JS, Montellier E, Buchou T, Cheng Z, Rousseaux S, Rajagopal N, *et al.* (2011). Identification of 67 histone marks and histone lysine crotonylation as a new type of histone modification. Cell 146, 1016–1028.

Tessarz P, Kouzarides T (2014). Histone core modifications regulating nucleosome structure and dynamics. Nat Rev Mol Cell Biol 15, 703–708.

Teves SS, Weber CM, Henikoff S (2014). Transcribing through the nucleosome. Trends Biochem Sci 39, 577–586.

Thirman MJ, Gill HJ, Burnett RC, Mbangkollo D, McCabe NR, Kobayashi H, Ziemin-van der Poel S, Kaneko Y, Morgan R, Sandberg AA, *et al.* (1993). Rearrangement of the MLL gene in acute lymphoblastic and acute myeloid leukemias with 11q23 chromosomal translocations. N Engl J Med 329, 909–914.

Torres EM, Williams BR, Amon A (2008). Aneuploidy: cells losing their balance. Genetics 179, 737–746.

Towbin BD, Gonzalez-Aguilera C, Sack R, Gaidatzis D, Kalck V, Meister P, Askjaer P, Gasser SM (2012). Step-wise methylation of histone H3K9 positions heterochromatin at the nuclear periphery. Cell 150, 934–947.

Ugarte F, Sousae R, Cinquin B, Martin EW, Krietsch J, Sanchez G, Inman M, Tsang H, Warr M, Passegue E, *et al.* (2015). Progressive chromatin condensation and H3K9 methylation regulate the differentiation of embryonic and hematopoietic stem cells. Stem Cell Rep 5, 728–740.

Venkatesh S, Workman JL (2015). Histone exchange, chromatin structure and the regulation of transcription. Nat Rev Mol Cell Biol 16, 178–189.

Vladimirova V, Mikeska T, Waha A, Soerensen N, Xu J, Reynolds PC, Pietsch T (2009). Aberrant methylation and reduced expression of LHX9 in malignant gliomas of childhood. Neoplasia 11, 700–711.

Weber CM, Henikoff S (2014). Histone variants: dynamic punctuation in transcription. Genes Dev 28, 672–682.

Weiner A, Lara-Astiaso D, Krupalnik V, Gafni O, David E, Winter DR, Hanna JH, Amit I (2016). Co-ChIP enables genome-wide mapping of histone mark co-occurrence at single-molecule resolution. Nat Biotechnol 34, 953–961.

Wickham H (2009). ggplot2: Elegant Graphics for Data Analysis, Dordrecht, Netherlands: Springer-Verlag.

Wike CL, Graves HK, Hawkins R, Gibson MD, Ferdinand MB, Zhang T, Chen Z, Hudson DF, Ottesen JJ, Poirier MG, *et al.* (2016). Aurora-A mediated histone H3 phosphorylation of threonine 118 controls condensin I and cohesin occupancy in mitosis. Elife 5, e11402.

Xing T, He H (2016). Epigenomics of clear cell renal cell carcinoma: mechanisms and potential use in molecular pathology. Chin J Cancer Res 28, 80–91.

Xu M, Wang W, Chen S, Zhu B (2012). A model for mitotic inheritance of histone lysine methylation. EMBO Rep 13, 60–67.

Yu T, MacPhail SH, Banath JP, Klokov D, Olive PL (2006). Endogenous expression of phosphorylated histone H2AX in tumors in relation to DNA double-strand breaks and genomic instability. DNA Repair (Amst) 5, 935–946.

Zane L, Sharma V, Misteli T (2014). Common features of chromatin in aging and cancer: cause or coincidence? Trends Cell Biol 24, 686–694.

Zee BM, Levin RS, Xu B, LeRoy G, Wingreen NS, Garcia BA (2010). In vivo residue-specific histone methylation dynamics. J Biol Chem 285, 3341x3350.

Zhang K, Tang H, Huang L, Blankenship JW, Jones PR, Xiang F, Yau PM, Burlingame AL (2002). Identification of acetylation and methylation sites of histone H3 from chicken erythrocytes by high-accuracy matrix-assisted laser desorption ionization-time-of-flight, matrix-assisted laser desorption ionization-postsource decay, and nanoelectrospray ionization tandem mass spectrometry. Anal Biochem 306, 259–269.

Zhang R, Poustovoitov MV, Ye X, Santos HA, Chen W, Daganzo SM, Erzberger JP, Serebriiskii IG, Canutescu AA, Dunbrack RL, *et al.* (2005). Formation of MacroH2A-containing senescence-associated heterochromatin foci and senescence driven by ASF1a and HIRA. Dev Cell 8, 19–30.

Zhao QY, Lei PJ, Zhang X, Zheng JY, Wang HY, Zhao J, Li YM, Ye M, Li L, Wei G, Wu M (2016). Global histone modification profiling reveals the epigenomic dynamics during malignant transformation in a four-stage breast cancer model. Clin Epigenetics 8, 34.